Stanford Exploration Project, Report 120, May 3, 2005, pages 197–216

Interpolation and signal extraction of teleseismic wavefields with the linear radon transform

Charles K. Wilson and Antoine Guitton[1]

ABSTRACT

We present a new method for data interpolation and signal/noise separation of teleseismic wavefields recorded by regional seismic arrays. The method exploits the plane wave nature of direct arrivals and receiver-side arrivals from regional scale structure by decomposing the recorded wavefield into a plane wave basis using the linear radon transform. Casting the radon transform as an inversion problem allows the incorporation of time dependent weighting schemes and model variance tuning which are helpful in minimizing artifacts related to the transform process while enhancing lower amplitude arrivals. Following radon transformation, we mute portions of the radon panel that represent plane waves with significantly different moveout ($\sim \pm .1$ s/km) relative to the direct arrival. Transformation back to the data domain from the muted radon domain gives the original signal without (1) plane waves following undesired moveouts, (2) white ambient noise, and/or (3) arrivals not represented well by plane waves (diffractions). Interpolation follows from the inverse data spray operation computed upon return to the data domain and the implicit assumption that a plane wave basis provides the most compact representation of the teleseismic wavefield.

INTRODUCTION

The growing abundance of densely sampled recordings of the teleseismic wavefield from regional scale portable and permanent seismic arrays demands the employment of more sophisticated array processing algorithms previously developed for seismic exploration. Most of the effort to date has concentrated on depth imaging algorithms using forward-scattered arrivals and free-surface multiples (Dueker and Sheehan, 1997; Sheehan et al., 2000; Rondenay et al., 2001; Aprea et al., 2002; Poppeliers and Pavlis, 2003; Wilson et al., 2003; Wilson and Aster, 2004). We suggest that imaging efforts in the absence of other preprocessing steps often are misguided. Seismic imaging algorithms are developed for noise-free datasets with an ideal distribution of source-receiver geometries that illuminate the imaging target from all angles. Even exploration data collected using industry standard acquisition geometries and well-controlled local sources with clean, easily modeled source functions are plagued by noise and incomplete illumination. To overcome these acquisition shortcomings, industry processing flows usually

[1]**email:** wilsonck@sep.stanford, antoine@sep.stanford.edu

begin with different combinations of deconvolution, data interpolation and regridding, surface static corrections, datuming, and spatial/temporal filtering (Yilmaz, 1997).

Although many arrivals in the teleseismic wavefield have comparable and sometimes better signal-to-noise ratios than exploration experiments, all teleseismic imaging experiments suffer from sparse, incomplete, and irregular angular and spatial sampling (e.g. limited range of source-receiver offsets and azimuths). These difficulties hamper imaging efforts and require the employment of preprocessing steps similar to those used by the exploration industry. Deconvolution in the form of traditional "receiver function analysis" is of course widely employed to enhance receiver-side converted arrivals (Phinney, 1964; Langston, 1977). Initial attempts to use f-k (Wilson and Aster, 2004) or Karhunen-Loeve (Rondenay et al., 2001) filtering on teleseismic data have shown promise although it may not be the best method of signal extraction because of lack of spatial frequency resolution and inability to cope with time variable (non-stationary) signals. Other preprocessing efforts have used the predicted teleseismic P-wave slowness for a given arrival to separate signal from near surface scattering (Jones and Phinney, 1998; Wilson et al., 2003, 2004) and to interpolate data traces (Poppeliers and Pavlis, 2003) . However, besides deconvolution, none of these or other widely used industry standard preprocessing steps have become commonplace in teleseismic imaging practice despite its apparent necessity.

It is likely that the exclusion of these preprocessing steps is largely historical. Initial analysis of teleseismic conversions was performed with a single set of three component seismograms recorded by an isolated station (Phinney, 1964; Langston, 1977). To avoid scattering from short wavelength features that depend strongly on back-azimuth, seismograms from single stations were routinely low-pass filtered to remove everything except energy primarily sensitive to structure with long spatial wavelengths (long temporal wavelengths). After the introduction of three component seismic arrays and with the birth of programs like IRIS-PASSCAL (http://www.iris.edu), data processing still followed the path devised for single isolated stations with the only difference being that the point measurements made by individual stations were now closer together. Much of the information about the lithospheric structure beneath the stations was discarded through temporal filtering and the absence of array-based processing. To extract the most information about lithospheric structure from increasingly more dense seismic arrays we must reexamine standard teleseismic data preprocessing flows prior to application of imaging algorithms.

For this reason, we have introduced a new method for signal/noise separation and data interpolation using an inverse formulation of the linear radon transform based on previous work applied to industry data (Sacchi and Ulrych, 1995; Guitton and Symes, 2003) . This paper will begin by defining signal and noise for wavefields produced by teleseismic earthquakes. After definition, we will show how differences in the basic moveout and geometry of the signal and noise wavefields can be used to separate them through projection of the data space onto a plane wave basis (linear radon domain). Our choice of separation through linear radon transform also gives us the added advantage of automatic data interpolation of spatially coherent plane wave arrivals upon return to the data domain. We show application of this technique to one synthetic and one recorded dataset with differing receiver spacing, target depths, and structural geometry.

COMPONENTS OF THE TELESEISMIC WAVEFIELD

The complete teleseismic wavefield (U_{total}) recorded at the surface can be represented as a linear combination of the impinging source wavefield (u_{src}), a specularly scattered wavefield (u_{spec}), a diffracted wavefield (u_{diff}), and an ambient noise wavefield (n) present at all times.

$$U_{total} = \underbrace{u_{src} + u_{spec}}_{SIGNAL} + \underbrace{u_{diff} + n}_{NOISE} \tag{1}$$

We assume either an isotropic character for the ambient noise (n) or that the highest amplitude components of the ambient noise wavefield (e.g. microseismic noise) do not follow the dominant moveout of teleseismic P wavefields. The speculary scattered portion of the wavefield contains plane wave arrivals generated at laterally continuous structures with little to no structural dip (arrivals marked A on Figure 1). The diffracted wavefield (arrivals marked B on Figure 1) consists of non-planar arrivals generated by point scatterers and short wavelength structures ($\leq$ 1/2 of the array aperture). For certain point scatterers, diffracted energy will arrive as plane waves that may appear as specularly scattered arrivals (arrivals marked C on Figure 1). In these instances, there will be no way to discriminate between a specularly scattered arrival from a planar,sub-horizontal interface and a diffraction except by comparing the scattered arrival slowness to that of the direct arrival.

THEORY OF NOISE ATTENUATION AND DATA INTERPOLATION USING RADON TRANSFORMS

Radon transforms are simple summations along predefined trajectories of the input data. These trajectories are controlled by a single parameter that defines the geometry of the summation trajectory. Various trajectories are chosen based on the input data with the most popular being the linear radon transform, the parabolic radon transform, or the hyperbolic radon transform. The choice of transform depends exclusively on the data to be processed. For instance, parabolic radon transforms are chosen for multiple attenuation of common mid-point gathers after normal move-out (Foster and Mosher, 1992). Hyperbolic radon transforms are most commonly used for producing velocity panels from seismic reflections following hyperbolic moveout (Taner and Koehler, 1969) but they can also be used for noise attenuation (Foster and Mosher, 1992) and data interpolation (Hindriks and Duijndam, 1998; Trad et al., 2002). In the teleseismic case, the plane wave nature of the data makes the use of linear radon transform a natural choice to process the data.

With the application of the linear radon transform we hope to extract the signal from the total wavefield and to interpolate the wavefield on return to the data domain. First, we intend to separate the signal and source wavefields from diffracted and ambient noise wavefields based on differences in slowness and wavefield curvature. Arrivals with a planar moveout will map well into the linear radon domain (see Figures 1 and 2). However, the diffuse ambient noise

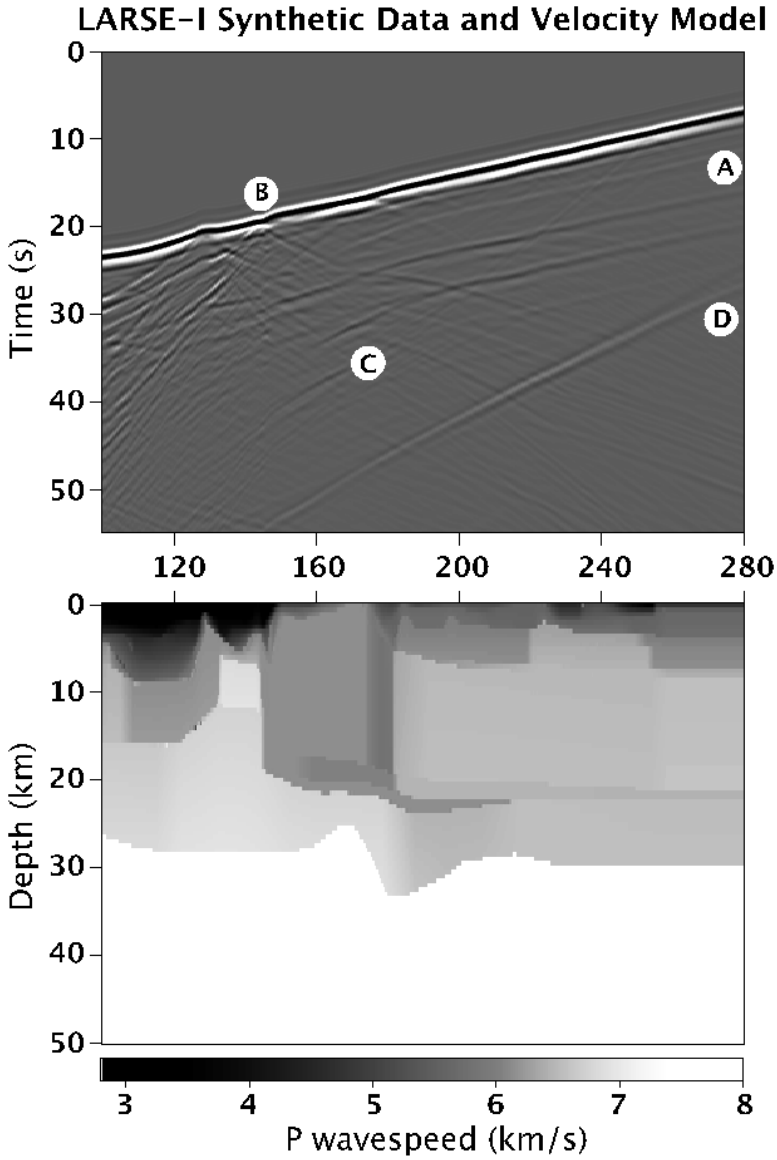

Figure 1: Synthetic seismograms (a) calculated from the LARSE-I velocity model (Baher et al., 2004) (b) generated by a steeply dipping incident plane wave from the base of the model (approximation of actual teleseismic source-receiver geometry). The arrivals marked (A) represent specularly scattered arrivals from laterally coherent structures. Notice these arrivals follow a similar moveout to the direct arrivals. Diffractions from both the bottom of the basin (B) and Moho topography (C) show a clearly different moveout and are slightly less planar than the direct arrival. The side reflection related to the boundary conditions of the synthetic model, marked as (D), approximates source-side scattered phases that have similar moveout to the direct arrival, such as pP. charlie1-Data+Model [NR]

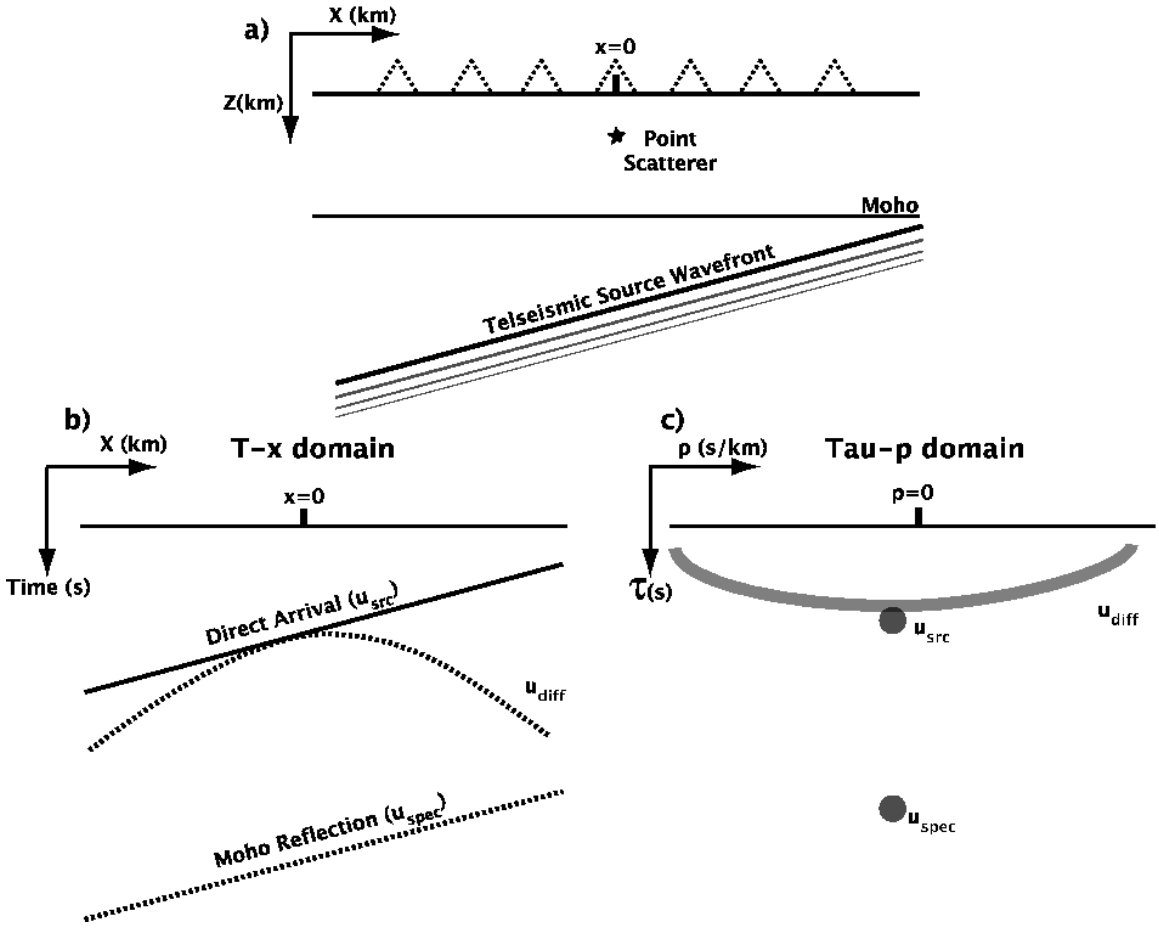

Figure 2: Figure showing representation of the teleseismic wavefield in the physical domain (a), the data domain (b), and the linear τ-p domain (c). By applying the linear radon transform we can differentiate between speculalrly scattered and diffracted waves as shown in (c). charlie1-TeleGeometry [NR]

wavefield and diffracted arrivals will have near zero amplitude after transformation because they are not represented well as plane waves. In the radon domain, coherent plane wave arrivals that do not follow the expected moveout of specularly scattered waves (e.g. P to Rg scattering from the surface and basin bottom topography) are assumed to be noise and muted. On return to the data domain, we will automatically interpolate the wavefield to a regularly sampled grid because of the plane wave representation of the wavefield and the loss of spatial reference in the radon domain.

Implementation of the linear radon transform

In this section, we show the details of the linear radon transform and how it can be cast as an inverse problem. The forward transformation maps the radon domain $m(\tau,s)$ into the data space $d(t,x)$ (recorded data) as follows:

$$d(t,x) = \sum_{s=s_{min}}^{s_{max}} m(\tau = t - sx, s), \tag{2}$$

and the adjoint transformation

$$m(\tau,s) = \sum_{x=x_{min}}^{x_{max}} d(t = \tau + sx, x), \tag{3}$$

where t is the time, x the station location (x_{min} and x_{max} being the offset range), s the slowness (s_{min} and s_{max} being the range of slownesses investigated), and τ the travel time at x_{min} (the first trace is the origin of the summation path).

Equation (2) can be rewritten in a more compact way by introducing the forward linear radon transform operator $\mathbf{L}$, the model space vector $\mathbf{m}$ (which contains all the $m(\tau,s)$ points) and the data vector $\mathbf{d}$ (which contains all the $d(t,x)$ points):

$$\mathbf{d} = \mathbf{L}\mathbf{m}. \tag{4}$$

Therefore, the goal is to minimize the difference between the input data $\mathbf{d}$ and the modeled data via the linear radon transform operator as follows:

$$\mathbf{0} = \mathbf{r_d} = \mathbf{L}\mathbf{m} - \mathbf{d}, \tag{5}$$

where $\mathbf{r_d}$ is called the data residual. As explained before, the data are irregularly spaced and traces may be missing. A mask $\mathbf{M}$ is introduced in equation (5) such that only the recorded data are considered in the residual:

$$\mathbf{0} = \mathbf{r_d} = \mathbf{M}(\mathbf{L}\mathbf{m} - \mathbf{d}), \tag{6}$$

where $\mathbf{M}$ is a diagonal operator that equals one where data are known and zero where they are unknown (at the missing traces). Finally, we estimate the radon domain by minimizing the objective function

$$f(\mathbf{m}) = \|\mathbf{r_d}\|^2, \tag{7}$$

which gives a least-squares estimate of the model parameters. Note that with the linear radon transform, the model space **m** can be estimated without inversion by introducing the so-called rho filter (Yilmaz et al., 1987), usually estimated in the Fourier domain. With missing traces, the rho filter is not appropriate anymore and inversion is required. In the next section, we describe how a sparse radon domain can be estimated with inversion.

Sparse inversion

For noise attenuation and data interpolation with radon transforms, numerous authors have shown that the inclusion of sparseness constraints during transformation into the radon domain improves the final result (Sacchi and Ulrych, 1995; Herrmann et al., 2000; Trad et al., 2003). The goal is to obtain a solution with minimum entropy (Burg, 1975). This property is important because radon transforms suffer from decreases in resolution due to the limited aperture of the data, creating transformation artifacts known as butterfly patterns (Kabir and Marfurt, 1999). The sparse inversion attenuates these effects by minimizing energy that does not focus well in the radon domain.

In this paper, we use the method of (Sacchi and Ulrych, 1995) to estimate a sparse model **m**. This technique imposes a Cauchy form probability-density function to the model parameters. This long-tailed probability-density function isolates the most energetic components of the radon domain and ignores the smallest, thus giving a minimum entropy solution. Note that other techniques such as stochastic inversion (Thorson and Claerbout, 1985) are also available.

To obtain a sparse radon domain **m**, a regularization term, i.e., the Cauchy function, is introduced in equation (7) as follows:

$$f(\mathbf{m}) = \|\mathbf{r_d}\|^2 + \epsilon^2 \sum_{i=1}^{N} \ln\left(1 + \frac{m_i^2}{\gamma^2}\right), \tag{8}$$

where N is the number of parameters to be estimated, ϵ the Lagrange multiplier and γ a parameter controlling the amount of sparseness in the model. Both ϵ and γ are estimated by trial and error. Whereas solving for **m** in equation (7) is a linear problem, solving for **m** equation (8) is not. Therefore, we use a quasi-Newton method to minimize iteratively the objective function in equation (8) (Guitton and Symes, 2003).

To demonstrate the effectiveness of the sparse radon transform for signal noise separation, we show the representation of the data panel from Figure 1 in the f-k domain (a), the radon domain (b), and the sparse radon domain (c). Much of the energy in the synthetic data panel follows linear moveout. Therefore, the dominant factor in real data for signal/noise separation becomes the moveout of the scattered arrival compared to the direct arrival. f-k filtering is effective at isolating energy with differing dips with proper spatial sampling but is unable to isolate the energy in time regardless of sampling geometry. The side reflection and the direct arrival are colocated in f-k space and can not be separated. In the radon domain, the side reflection and the direct arrivals map to distinctly different dips for different τ's. But, without sparseness constraints many spurious artifacts are introduced from unwanted arrivals. The

shaded region near zero slope represents an example radon mute that would remove the side reflection without reducing energy following the moveout of the direct arrival.

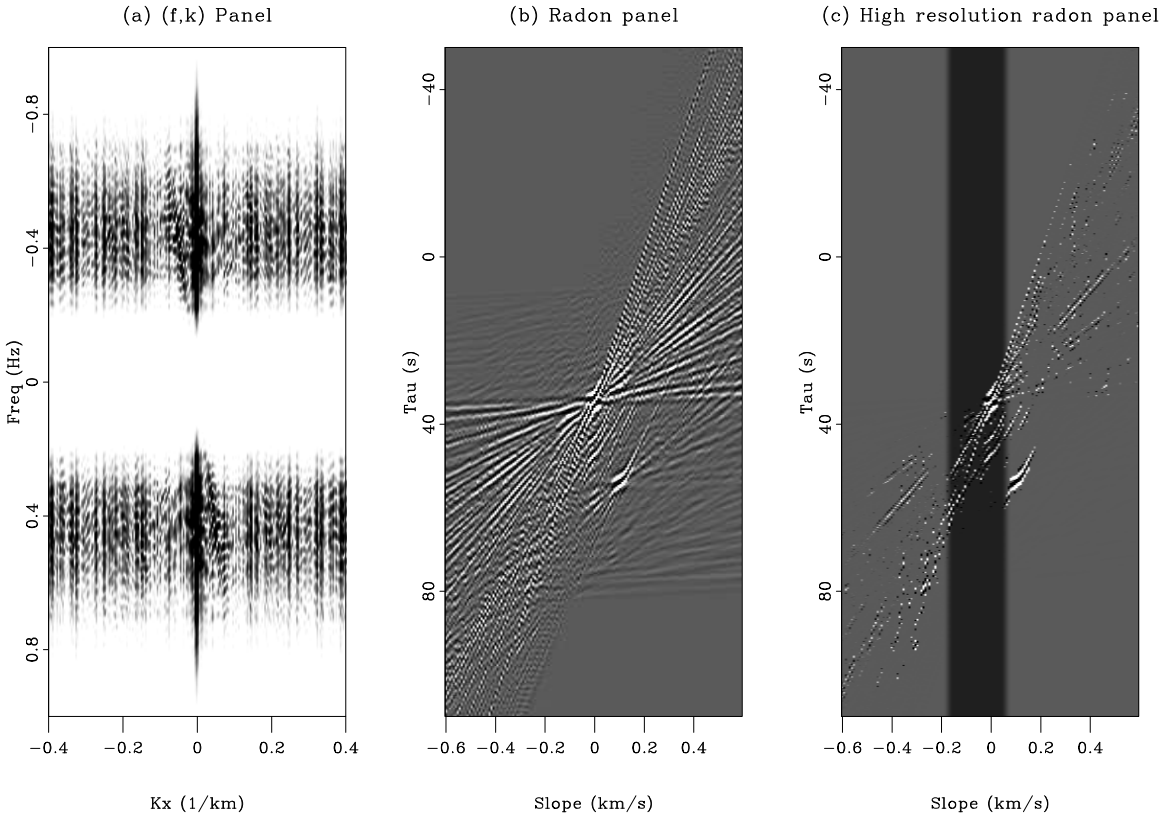

Figure 3: Figure showing representation of the synthetic teleseismic wavefield shown in 1 in the f-k domain (a), the radon domain (b), and the sparse linear radon domain (c). The letters denote arrival location identified in Figure 1. The f-k domain allows the isolation of distinct dips but does not offer a way to isolate different dips in time (e.g. time variable dip filter). The standard linear radon domain offers the possibility of separating dips as a function of time but introduces artifacts related to the transform. The sparse linear radon transform (c) allows us to isolate energy in time as in (b) while minimizing artifacts introduced from the transform. The shaded region indicates the radon mute used for the synthetic example shown in Figure 5. charlie1-complarse-fp-tp [NR]

Data interpolation and noise removal

Applying a mask in equation (6) eliminates the contribution of the empty traces in the model space, making them invisible to the inversion. Therefore, by simply remodeling a data panel from the estimated model $\hat{\mathbf{m}}$ after inversion without the mask, the missing traces are reconstructed. Then, the interpolated data vector $\mathbf{d_{int}}$ can be estimated as follows:

$$\mathbf{d_{int}} = \mathbf{d} + (\mathbf{I} - \mathbf{M})\mathbf{L}\hat{\mathbf{m}}, \tag{9}$$

where **I** is the identity matrix. Now, for the noise removal, we simply (1) apply a mute **K** in the radon domain that isolates and preserves the signal, and (2) transform the muted panel in the data space as follows:

$$\mathbf{n_{est}} = \mathbf{MLK}\hat{\mathbf{m}}, \tag{10}$$

where $\mathbf{n_{est}}$ is the estimated signal (specular reflections and impinging source). The estimated noise $\mathbf{n_{est}}$ (diffracted energy and ambient noise) is obtained by subtracting the estimated signal from the input data:

$$\mathbf{s_{est}} = \mathbf{d} - \mathbf{MLK}\hat{\mathbf{m}}. \tag{11}$$

Note that the estimated noise and signal in equations (10) and (11) are for the non-interpolated data. To compute the estimated noise and signal for the interpolated data, **M** must be removed in equations (10) and (11) and **d** must be replaced by $\mathbf{d_{int}}$ in equation (11).

SYNTHETIC TEST: DATA INTERPOLATION AND SIGNAL EXTRACTION

In this section, we show the results of applying the sparse linear radon transform to synthetic teleseismic waveforms calculated with a velocity model (Figure 1) from the LARSE-I experiment (Baher et al., 2004). This model presents several real challenges in the form of large gradients in wavespeed found at the bottom of the Los Angeles basin, in the mid and the lower crust beneath the surface trace of the San Andreas, and at the base of the San Gabriel Mountains. After synthetic calculation, we extracted seismograms with actual station event geometries recorded during the experiment. This provides us a test dataset where we have prior knowledge of the crustal structure for assistance in identification of signal and noise phases and accurately sampled data for later comparison following interpolation.

Figure 4 shows the results of interpolation (c) of the resampled (b) data panel presented in (a) using the high resolution linear radon transform. The resampled synthetic data panel mimics the actual recording geometry used in the LARSE-I experiment and demonstrates the effect of wavefield aliasing due to irregular and coarse sampling. Despite the somewhat extreme spatial aliasing, the interpolated wavefield (c) contains many of the major features seen in (a) including the specularly scattered phases seen clearly between 200-240 km (see Figure 1 for a more complete description), the high amplitude laterally coherent source wavefield, and the side reflection starting at 50 seconds at 280 km. In regions of especially sparse sampling, the amplitude of the interpolated data is slightly lower than in the original data panel and several butterfly artifacts can be identified. This suggests that finer, regular sampling would produce a more accurate and smooth data interpolation for many cases. Diffracted phases with large dips scattered from the basin bottom and the sharp Moho topography are severely aliased after resampling. For this example, we have applied a mute in the radon domain to regions outside of -0.18/0.05 s/km. This mute effectively removes surface scattered phases with large negative slopes and the side reflection with a positive slope near 0.1 s/km (Figure 5).

In Figure 5, we show the estimated signal from the synthetic data panel using both the linear radon transform (a and b) and standard f-k filtering (c). The comparison of the filtered signal using the interpolated traces (b) and all traces demonstrates how incomplete and

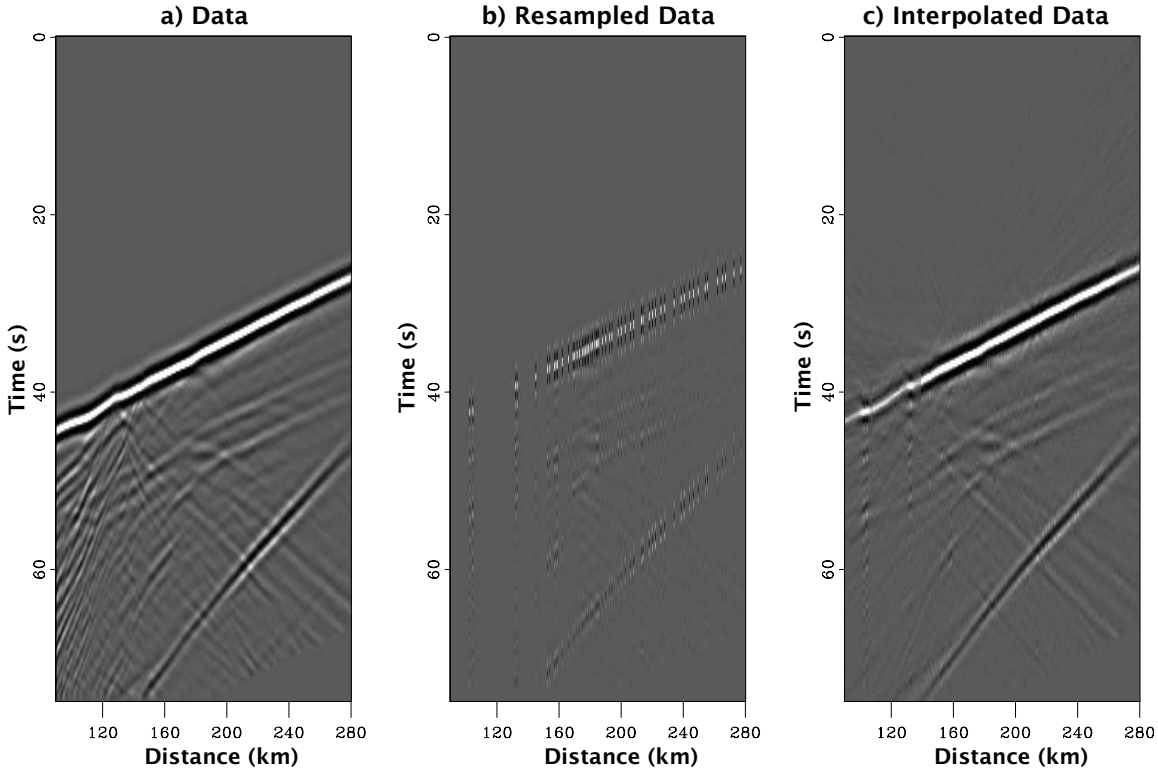

Figure 4: Results of interpolation (c) of synthetic data (a) decimated to station spacing similar to that employed in the LARSE experiment (b). The decimated data panel shows how spatial aliasing can significantly hamper the ability to recover structure easily seen in the data in panel (a). Interpolation recovers many of the major planar arrivals especially in the regions with adequate sampling. charlie1-SynthData-Result [NR]

irregular spatial sampling (e.g most teleseismic experiments) severely effects all procedures attempting to estimate and filter dips. Both the f-k and high resolution linear radon transform produce good results when the wavefield is adequately sampled. Unfortunately, this is rare and f-k methods do not offer an interpolation method except in cases of evenly spaced sampling. The filtered, interpolated data shown in panel (b) retains the medium to long wavelength, laterally coherent structures with similar moveout to the direct arrival. The majority of contamination from shallow scattering occurs in the region between 100-140 km. This is also the region of the poorest sampling and makes dip filtering very difficult. Therefore, some of what might be considered signal is lost in this area.

The linear radon transform excels in a few important areas of the data pnale when compared to the f-k filtered data panel. This is directly related to the suprerior dip and time resolution in the radon domain as compared to f-k space. For example, Moho diffraction tails seen between 160-180 km at $\sim$50 seconds are lost in the f-k section and remain in both radon filtered sections. Depending on the imaging algorithm chosen these diffraction tails could be considered signal or noise. A tighter mute in the radon domain could remove these features if necessary. This type of flexibility is not available with f-k filtering. Also, note the presence of the side reflection in the f-k filtered sections and its absence in the Radon filtered panels. Identification of the side reflection can occur in the f-k domain however separating without removing signal is difficult without using other attributes such as arrival time.

Possibly the easiest way to determine the effectiveness of the filtering operation is to look at what remains after subtracting the filtered section from the raw data (see Figure 6). This provides a visual measure of what was removed and subsequently classified as noise. Figure 6 shows the difference panels from high resolution radon filtering of all traces (a) and interpolated traces (b) and f-k filtering of all traces (c). The f-k panel was most effective with the near surface scattered energy although, the diffraction tails absent from the signal panel 5 have reemerged here in the noise panel. Much of the major noise features are present on the noise estimates created with complete data panels (a and c). However, the interpolated data panel fails to identify a significant amount of energy from shallow features (near 40 s and between 100-140 km) as noise. Most likely this is because of dip ambiguities that result from coarse and irregular sampling. Ambiguous dips in a data panel are spread across a broader region in the radon domain and can not be completely muted.

APPLICATION TO CASCADIA TELESEISMIC DATA

The Cascadia seismic array deployed during 1993-1994 (Nabelek et al., 1993), recorded data that was later used to make remarkable images of the underlying subduction zone (Rondenay et al., 2001; Bostock et al., 2002). These data assisted in demonstrating the potential of producing high quality images with regularly and densely sampled teleseismic wavefields. We show the results of application of the high resolution linear radon transform to the P and Sv component for one event from the recorded data (Figure 7). We chose an example event from this dataset because of its dense, approximately regular sampling and because the scattered wavefield contains clearly discernible arrivals with time variable dips. We feel that although this dataset

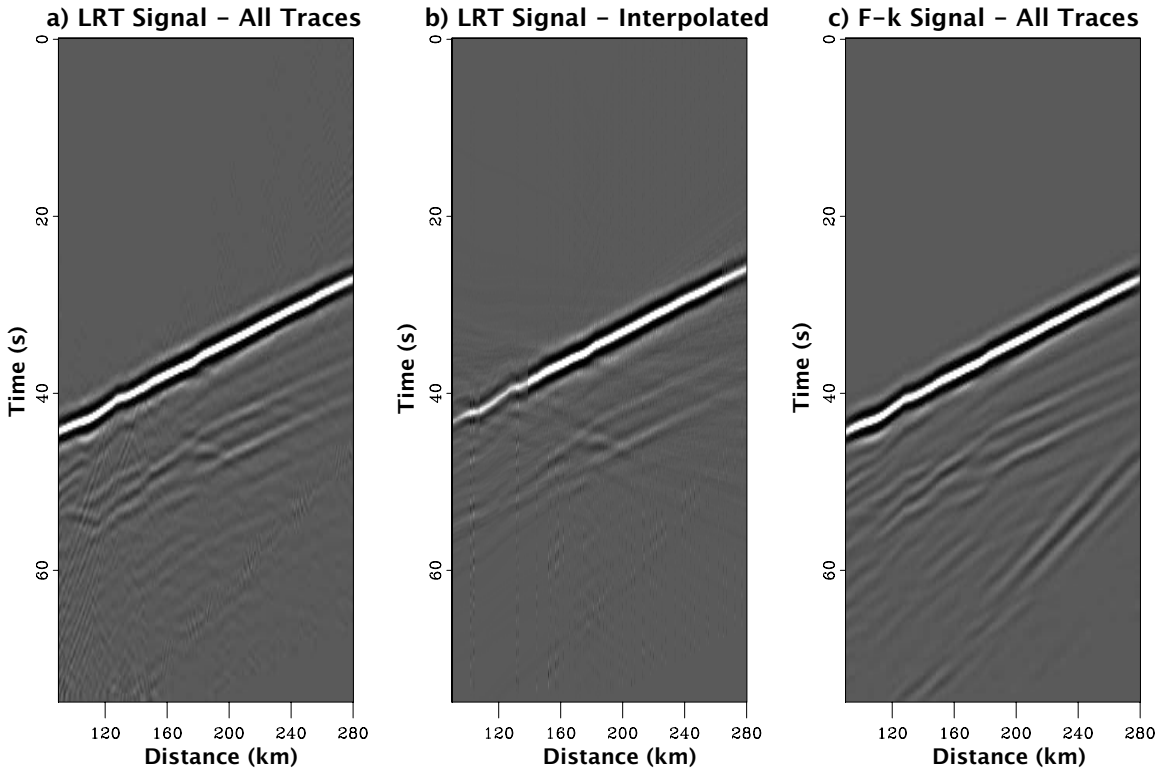

Figure 5: Comparison of signal panels calculated using the linear radon transform with all traces (a), linear radon transform with realistic station geometry (b), and f-k filtering using all traces. The results using the linear radon transform effectively muted the side reflection although this was not possible with f-k filtering without significantly degrading the signal. Diffraction tails from the complicated Moho topography between 160-200 km at 50 seconds have been removed by f-k filtering and replaced by artificial laterally continuous arrivals. The true character of these arrivals have not been modified by the radon algorithm although they could be removed with a modified mute window. charlie1-SynthSignal-Result [NR]

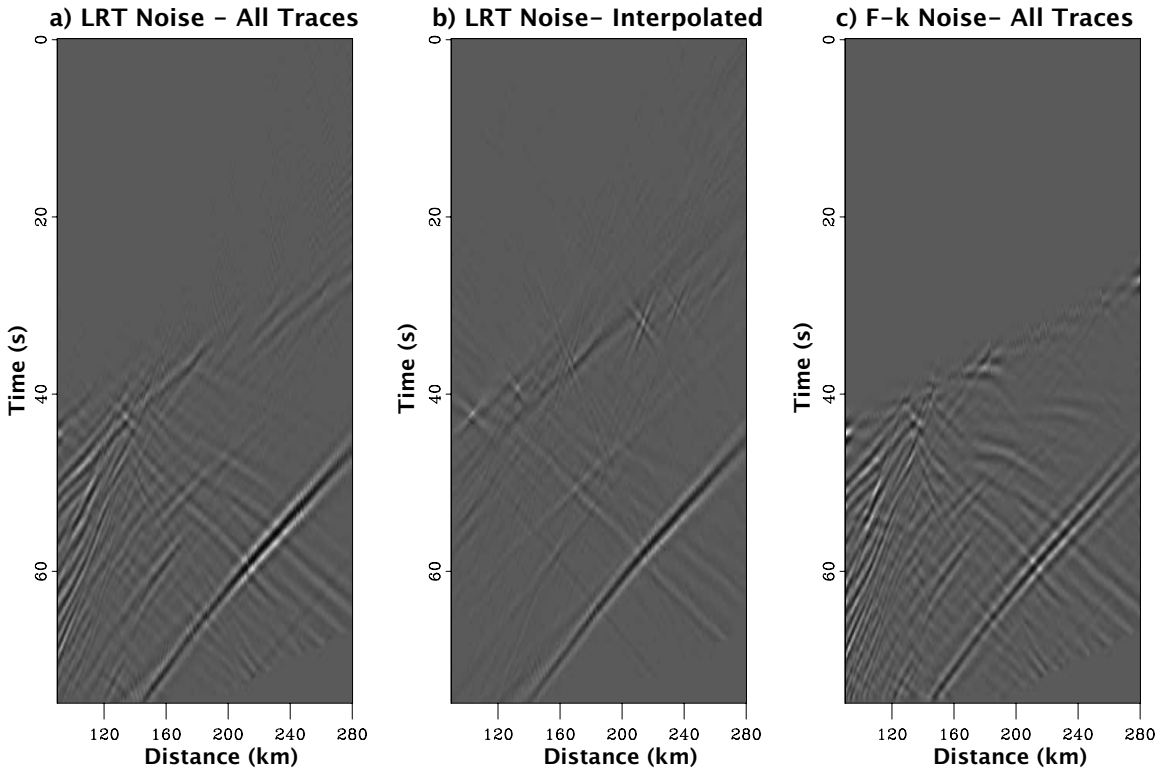

Figure 6: Comparison of noise panels calculated by subtracting results shown in Figure 5 from the original data panels shown in Figure 4. The truncated diffraction tails from the complicated Moho topography between 160-200 km at 50 seconds removed by f-k filtering have reappeared in the noise panels. The f-k filter was able to remove some of the energy from the side reflection (clearly seen in the noise panel) but this is still a significant arrival in Figure 5c. We prefer the noise estimation shown in (a) and (b) because we feel the character of the actual data and the noise have not been affected by spurious truncations and artifacts apparent in the f-k panels. charlie1-SynthNoise-Result [NR]

makes an excellent example it is not an isolated case and this method would be effective with other densely sampled datasets.

Figure 7 shows a high resolution radon panel of the P component (Figure 7a) followed by the recorded data (Figure 7b) , the estimated signal (Figure 7c), and the estimate noise panel (Figure 7d). The radon panel (Figure 7a) shows the clearly focussed direct P arrival beginning centered around 0 s/km, near 30 seconds. It is followed by lower amplitude coda waves until near 120 seconds. At 120 seconds, there is a clear change in primary slowness to a peak centered at $\sim$0.04 s/km. We interpret this arrival as pP because of its timiCASC-Png and its similar slowness and character to that of the direct arrival. After application of the radon mute (white panel in Figure 7c), the arrival was successfully removed and the underlying coda of the direct P arrival is recovered (Figure 7c). The estimated noise wavefield contains the majority of the energy from the later arrival as well as some low amplitude arrivals with negative dips recorded just after the direct arrival. By examining similarities between the signal and noise wavefields we can estimate cross-contamination of arrival dips in each wavefield and evaluate the quality of our taper parameters. In this case (Figure 7), the estimated signal and noise show little similarity and are comprised by a set of arrivals with distinctly different dips. This supposition is demonstrated by the clear separation of arrivals in the radon domain.

Figure 8 shows the same panels as in Figure 7 but for the Sv component from the same event. In this case, the small relative amplitude difference between diffracted noise and specularly scattered arrivals directly following the direct P arrival makes foccusing energy in the radon domain difficult. Despite the limited focussing in the radon domain, application of the radon mute clearly separates arrivals with differing dips which are intermingled near 70 seconds (see panel 8b). These arrivals are visible as low amplitude radon peaks at 0.08 s/km near 45 seconds and 0.2 s/km at 70 seconds (8a). These represent the forward scattered and free-surface reflected arrivals from the dipping subducting slab below. By muting dips greater than 0.2 s/km we can remove this free-surface reflection as demonstrated in the estimated noise panel in Figure 8c. The absence of coherent features in the estimated noise panel (Figure 8d) other than the energy beginning between 60 and 90 seconds indicates that we the mute successfully separates the forward and back-scattered wavefields. This example also demonstrated the potential of using the radon transform as a wavefield separation technique regardless of the relative amplitude between the wavefields identified as signal and noise.

CONCLUSIONS

We have introduced a method of separating signal and noise and interpolating irregularly sampled data from regional scale teleseismic recordings using application of industry standard filtering algorithms based on the linear radon transform. With this method, we exploit the plane wave nature of much of the teleseismic wavefield useable for creating structural images of the lithosphere. Arrivals not following plane wave moveouts, within a desired dip range, are easily identified and removed from the recorded wavefield. Additionally, the linear radon transform provides a method for interpolation of planar arrivals that reside within the desired dip range.

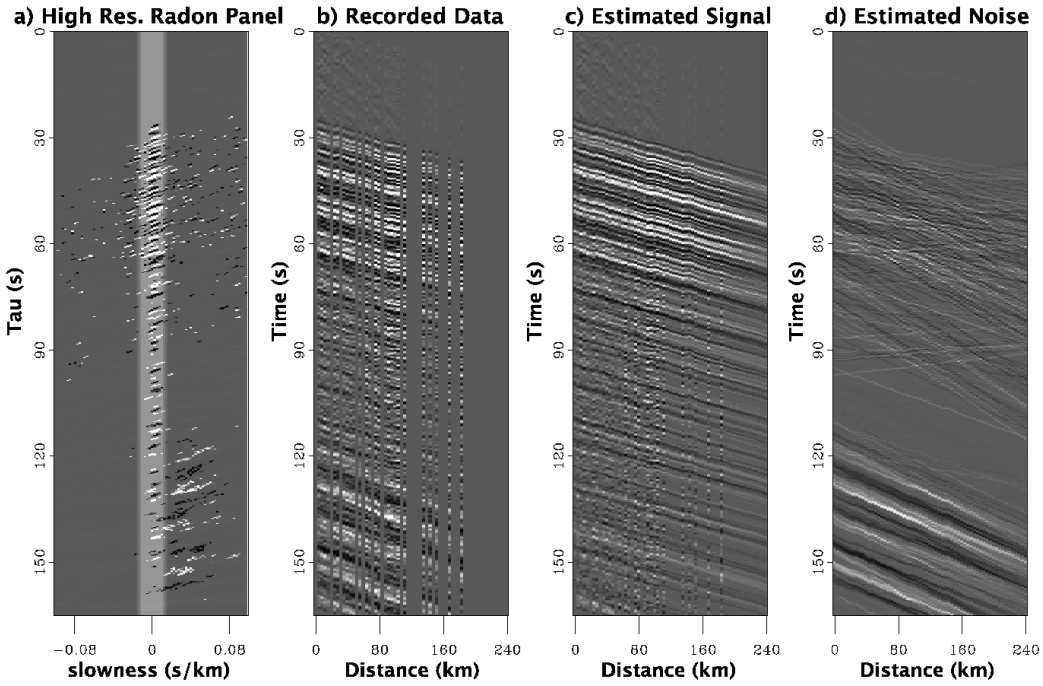

Figure 7: Figure showing the (a) high resolution radon panel of the P component, (b) the recorded data, (c) the estimated signal, and (d) the estimated noise panel (Figure 7d) for an event recorded by the Cascadia seismic array. This radon panel (a) shows how time variable dips can be used to separate wavefields that are coincident in time. The resulting interpolated panel (c) does not contain dips significantly different from that of the direct arrival (seen in panel (d)). charlie1-CASC-P [NR]

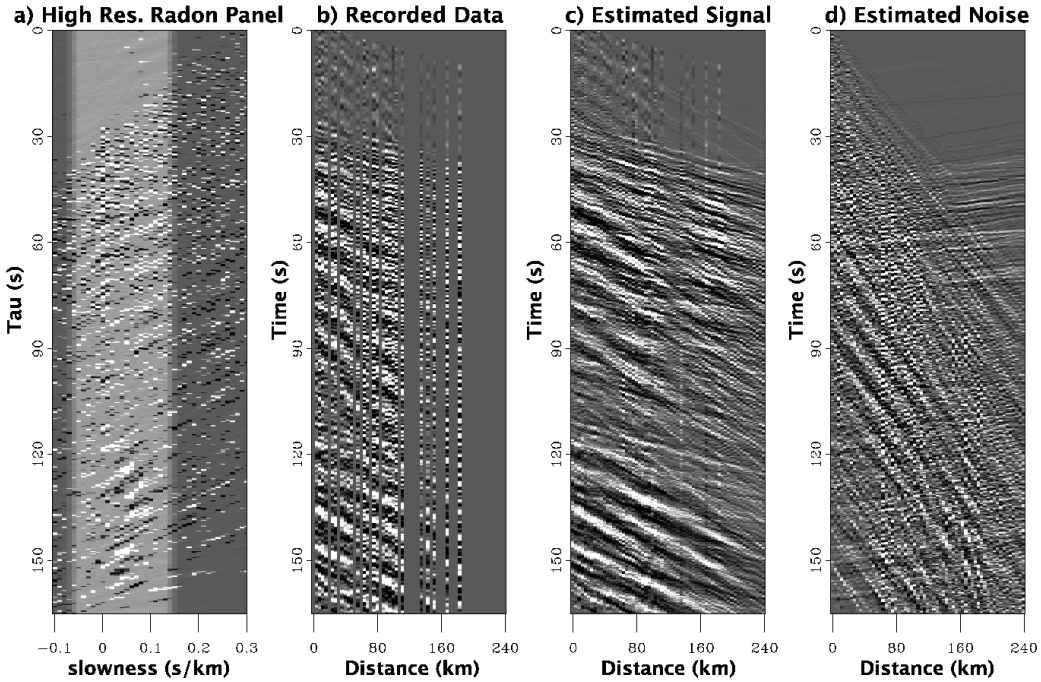

Figure 8: Figure showing the (a) high resolution radon panel of the Sv component, (b) the recorded Sv data, (c) the estimated signal, and (d) the estimated noise panel (Figure 8d) for an event recorded by the Cascadia seismic array. The radon panel appears to be poorly focussed until later τ. Despite the lack of focus, application of the radon mute allows the separation of the arrivals with clearly different dips near 60 seconds. charlie1-CASC-Sv [NR]

We have shown the method to be successful in interpolating real data and synthetic data with a real acquisition geometry created with a complicated wavespeed model. In addition, we have shown this method to be effective at isolating dips differing from the laterally coherent scattering and source related energy even in the presence of severe under sampling. We have demonstrated that our method is more effective than f-k filtering because it has superior dip resolution, allows the separation of dips as a function of time, and can handle (and interpolate) irregular wavefield sampling. Besides the algorithm development, the most important aspect of this study has been the recognition of the effect of current standard teleseismic wavefield acquisition geometries on dip filtering as well as standard seismic imaging methods. We hope that the examples shown in this paper will motivate denser deployments in the future to allow proper pre-processing and insure more accurate images than are presently possible.

REFERENCES

Aprea, C. M., Hildebrand, S., Fehler, M., Steck, L., Baldridge, W. S., Roberts, P., Thurber, C. H., and Lutter, W. J., 2002, Three-dimensional Kirchhoff migration: Imaging of the Jemez volcanic field using teleseismic data: J. Geophys. Res., **107**, no. B10, doi: 10.1029/2000JB000097.

Baher, S., Fuis, G., Wilson, C., Langenheim, V., and Murphy, J., 2004, The Onshore-Offshore LARSE I Transect: San Clemente Island to the Mojave Desert–Crustal blocks and the Moho: Eos Trans. AGU, **85 (47)**, Fall Meet. Suppl., Abstract S53B–0206.

Bostock, M. G., Hyndman, R. D., Rondenay, S., and Peacock, S. M., 2002, An inverted continental Moho and serpentinization of the forearc mantle: Nature, **417**, no. 6888, 536–538.

Burg, J. P., 1975, Maximum Entropy Spectral Analysis: Ph.D. thesis, Stanford University.

Dueker, K. G., and Sheehan, A. F., 1997, Mantle discontinuity structure from midpoint stacks of converted P to S waves across the Yellowstone hotspot track: J. Geophys. Res., **102**, no. B4, 8313–8327.

Foster, D. J., and Mosher, C. C., 1992, Suppression of multiple reflections using the Radon transform: Geophysics, **57**, no. 03, 386–395.

Guitton, A., and Symes, W., 2003, Robust inversion of seismic data using the Huber norm: Geophysics, **68**, no. 4, 1310–1319.

Herrmann, P., Mojesky, T., Magesan, M., and Hugonnet, P., 2000, De-aliased, high-resolution Radon transforms: Soc. of Expl. Geophys., 70th Ann. Internat. Mtg, 1953–1956.

Hindriks, C. O. H., and Duijndam, A. J. W., 1998, Radon domain reconstruction of 3-D irregularly sampled VSP data: Soc. of Expl. Geophys., 68th Ann. Internat. Mtg, 2003–2006.

Jones, C. H., and Phinney, R. A., 1998, Seismic structure of the lithosphere from teleseismic converted arrivals observed at small arrays in the southern Sierra Nevada and vicinity, California: J. Geophys. Res., **103**, no. B5, 10065–10090.

Kabir, M. M. N., and Marfurt, K. J., 1999, Toward true amplitude multiple removal: The Leading Edge, **18**, no. 1, 66–73.

Langston, C. A., 1977, Effect of Planar Dipping Structure on Source and Receiver Responses for Constant Ray Parameter: Bulletin of the Seismological Society of America, **67**, no. 4, 1029–1050.

Nabelek, J., Li, X.-Q., Azevedo, S., Braunmiller, J., Fabritius, A., Leitner, B., Trehu, A. M., and Zandt, G., 1993, A high-resolution image of the cascadia subduction zone from teleseismic converted phases recorded by a broadband seismic array: Eos Trans. AGU, **74(43), Fall Meet. Suppl.**

Phinney, R. A., 1964, Structure of the Earth's Crust from Spectral Behavior of Long-Period Body Waves: J. Geophys. Res., **69**, no. 14, 2997–3017.

Poppeliers, C., and Pavlis, G. L., 2003, Three-dimensional, prestack, plane wave migration of teleseismic P-to-S converted phases: 1. Theory: J. Geophys. Res., **108**, no. B2, art. no.–2112.

Rondenay, S., Bostock, M. G., and Shragge, J., 2001, Multiparameter two-dimensional inversion of scattered teleseismic body waves 3. Application to the Cascadia 1993 data set: J. Geophys. Res., **106**, no. B12, 30795–30807.

Sacchi, M. D., and Ulrych, T. J., 1995, High-resolution velocity gathers and offset space reconstruction: Geophysics, **60**, no. 04, 1169–1177.

Sheehan, A. F., Shearer, P. M., Gilbert, H. J., and Dueker, K. G., 2000, Seismic migration processing of P-SV converted phases for mantle discontinuity structure beneath the Snake River Plain, western United States: J. Geophys. Res., **105**, no. B8, 19055–19065.

Taner, M. T., and Koehler, F., 1969, Velocity spectra - Digital computer derivation and applications of velocity functions: Geophysics, **34**, no. 06, 859–881.

Thorson, J. R., and Claerbout, J. F., 1985, Velocity stack and slant stochastic inversion: Geophysics, **50**, no. 12, 2727–2741.

Trad, D., Ulrych, T. J., and Sacchi, M. D., 2002, Accurate interpolation with high-resolution time-variant Radon transforms: Geophysics, **67**, no. 2, 644–656.

Trad, D., Ulrych, T., and Sacchi, M., 2003, Latest views of the sparse Radon transform: Geophysics, **68**, no. 1, 386–399.

Wilson, D. C., and Aster, R. C., 2004, Receiver function seismic imaging of the crust and upper mantle using frequency-wavenumber filtering and regularized multimode kirchhoff migration: Eos Trans. AGU, **85(47)**, Fall Meet. Suppl., Abstract S33A–1090.

Wilson, C. K., Jones, C. H., and Gilbert, H. J., 2003, Single-chamber silicic magma system inferred from shear wave discontinuities of the crust and uppermost mantle, Coso geothermal area, California: J. Geophys. Res., **108**, no. B5, art. no.–2226.

Wilson, C. K., Jones, C. H., Molnar, P., Sheehan, A. F., and Boyd, O., 2004, Distributed deformation in the lower crust and upper mantle beneath a continental strike-slip fault zone: Marlborough Fault System, South Island, New Zealand: Geology, **32**, 837–840.

Yilmaz, O., Chambers, R., Nichols, D., and Abma, R., 1987, Fundamentals of 3-D Migration: The Leading Edge, **6**, 22–30.

Yilmaz, O., 1997, Seismic Data Processing:, volume 2 of **Investigations in Geophysics** Society of Exploration Geophysics, Tulsa, Oklahoma.